

# Structural evolution in transitional nuclei of mass $82 \leq A \leq 132$

M. Bhuyan<sup>\*</sup>

*State Key Laboratory of Theoretical Physics, Institute of Theoretical Physics, Chinese Academy of Sciences, Beijing 100190, China*

(Received 19 January 2015; revised manuscript received 27 July 2015; published 22 September 2015)

In this theoretical study, we report an investigation on the behavior of two-neutron separation energy, a differential variation of the nucleon separation energy, the nuclear charge radii, and the single-particle energy levels along the isotopic chains of transitional nuclei. We have used the relativistic mean-field formalism with NL3 and NL3\* forces for this present analysis. The study refers to the even-even nuclei such as Zr, Mo, Ru, and Pd for  $N = 42-86$ , where a rich collective phenomena such as proton radioactivity, cluster or nucleus radioactivity, exotic shapes, island of inversion, etc. are observed. We found that there are few nonmonotonic aspects over the isotopic chain, which are correlated with the structural properties such as shell/subshell closures, the shape transition, clustering, magicity, etc. In addition to these, we have shown the internal configuration of these nuclei to get a further insight into the reason for these discrepancies.

DOI: [10.1103/PhysRevC.92.034323](https://doi.org/10.1103/PhysRevC.92.034323)

PACS number(s): 21.10.Dr, 21.10.Ft, 21.10.Gv, 21.10.Tg

## I. INTRODUCTION

Nowadays, one of the most sensitive and crucial regions in the nuclear chart for investigation lies between  $Z = 35-64$  and  $A = 82-132$ . This region reveals a large number of interesting discoveries of new phenomena, such as proton radioactivity [1–3], cluster radioactivity [4–6], exotic shapes [7,8], island of inversion [9,10], abnormal variation of major shell closures (i.e., extra stability near drip line) [11–13], giant halo near neutron drip-line region [14], etc. These crucial features may be due to the rapidly growing possibility of the neutron-proton ratio ( $N/Z$ ) in a nucleus. From the last few decades, it is possible to study these exotic nuclei by using the radioactive isotope beam (RIB) facilities. This reveals the concept entitled, as aforementioned, magic number. In other words, the confirmation of magic numbers near the  $\beta$ -stability line is not mandatory universal [15–17]. Further, the structural properties of nuclei far away from the  $\beta$ -stability line are also active areas of research in both theories and experiments [13,14,18]. In particular, the neutron-rich Zr–, Mo–, Ru–, and Pd– with mass numbers  $A = 100-130$  are of special interest for various reasons. For example, they lie far away from the  $\beta$ -stable region of the nuclear landscape, resulting in a well-established deformation, but close enough in the magnitude of microscopic excitations to compete with the collectivity of double shell closure nuclei [14,19,20]. Moreover, these nuclei are also holding an active participation in the nucleosynthesis of heavy nuclei in the astrophysical  $r$  process. The mass and decay properties are quite an essential ingredient to building up the path, the isotopic abundances, and the time period of these process [21].

In addition to that, the nuclear structure of these nuclei is characterized by a strong competition between various shapes, which gives rise to the shape instabilities that lead to coexisting nuclear shape transitions in the isotopic chains [22]. This could be understood from the potential energy surface at different deformations. Elaborately, the occurrence of two (or more)

nearly equally deep minima in the potential energy surface at different deformations shows the signature for nuclear shape coexistence. Hence, one can say the nuclear shapes not only vary with the nucleon number but also with the excitation energy and spin. It is well known that the binding energy of a nucleus is one of the most precisely measured observable from the experiments [23,24]. Several nuclear observables, which are highly relevant for understanding various features of the nuclear structure, can be computed from its mass, such as the average nuclear field, nucleon-nucleon (NN) potential, single-particle energy, etc. The correlations among these fundamental quantities are amended to explain the deformed ground states, low-lying isomeric states, and few derived quantities, such as moments of inertia and vibrational excitation energy, etc. [25–28]. It is acclaimed that the energy involved in the removal of fermions from a strongly correlated system of identical fermions must be a good indicator for the stability of the system. The magnitude of this energy has much higher values for systems with an even number of particles than an odd one, if the pairing is a dominant component in the binary fermion-fermion interaction.

In the present work, the quantities of interest are the nuclear potential energy surface, nuclear shape, nuclear binding energy, two-neutron separation energies ( $S_{2n}$ ), the differential variation of neutron separation energy  $\Delta S_{2n}$ , the root-mean-square charge distribution  $r_{ch}$ , and the single-particle energy level for the even-even mass transition nuclei. Based on these decisive observables, we have focused on the evolution of the structural properties of transition nuclei. The paper is organized as follows: Sec. II gives a brief description of the relativistic mean-field formalism including the pairing energy correlation. The results of our calculations along with discussions are presented in Sec. III. Section IV includes a short summary along with a few concluding remarks.

## II. RELATIVISTIC MEAN-FIELD (RMF) METHOD

From the last few decades, the nuclear covariant density functional theories (CDFTs) are quite successful in describing the ground and the intrinsic excited state, including fission

\*bunuphy@itp.ac.cn

TABLE I. The center-of-mass energy obtained from phenomenological [58] and microscopic self-consistent methods [59,60] for Zr isotopes.

Method	$^{100}\text{Zr}$	$^{102}\text{Zr}$	$^{104}\text{Zr}$	$^{106}\text{Zr}$	$^{108}\text{Zr}$	$^{110}\text{Zr}$	$^{112}\text{Zr}$	$^{114}\text{Zr}$	$^{116}\text{Zr}$	$^{118}\text{Zr}$	$^{120}\text{Zr}$
$E_{\text{c.m.}} = \frac{3}{4}A^{-\frac{1}{3}}$	-6.63	-6.58	-6.54	-6.46	-6.46	-6.42	-6.38	-6.34	-6.31	-6.27	-6.23
$E_{\text{c.m.}} = \frac{\langle F   P^2   F \rangle}{2M}$	-6.83	-6.79	-6.75	-6.68	-6.61	-6.55	-6.49	-6.45	-6.41	-6.44	-6.47

states of the exotic heavy and superheavy nuclei over the nuclear chart [29–36]. Basically, there are four different patterns to perform the covariant density functional: the point coupling nucleon or meson exchange interactions connected with the density-dependent or nonlinear couplings. One can also introduce all shape degrees of freedom to CDFTs by breaking both the axial and reflection symmetries simultaneously (see Ref. [34] for more details). In the relativistic mean-field approach, the nucleus is considered as a composite system of nucleons (proton and neutron) interacting through exchanges of mesons and photons [31,37–42]. Further, the contributions from the meson fields are described either by mean fields or by pointlike interactions between the nucleons [43,44], and the density-dependent coupling constants [45,46] or nonlinear coupling terms [47,48] are introduced to reproduce the correct saturation properties of infinite nuclear matter. Here, most of the computational efforts are devoted to solving the Dirac equation and to calculate various densities. In the present calculations, we have used the microscopic self-consistent relativistic mean-field (RMF) theory as a standard tool to investigate the nuclear structure phenomena. It is worth mentioning that the RMF approach is one of the most popular and widely used formalisms among them. The relativistic Lagrangian density (after several modification of the original Walecka Lagrangian to take care of various limitations) for a nucleon-meson many-body system [37–42,49–53] is given as:

$$\begin{aligned} \mathcal{L} = & \overline{\psi}_i \{i\gamma^\mu \partial_\mu - M\} \psi_i + \frac{1}{2} \partial^\mu \sigma \partial_\mu \sigma - \frac{1}{2} m_\sigma^2 \sigma^2 \\ & - \frac{1}{3} g_2 \sigma^3 - \frac{1}{4} g_3 \sigma^4 - g_s \overline{\psi}_i \psi_i \sigma - \frac{1}{4} \Omega^{\mu\nu} \Omega_{\mu\nu} \\ & + \frac{1}{2} m_w^2 V^\mu V_\mu - g_w \overline{\psi}_i \gamma^\mu \psi_i V_\mu - \frac{1}{4} \vec{B}^{\mu\nu} \cdot \vec{B}_{\mu\nu} \\ & + \frac{1}{2} m_\rho^2 \vec{R}^\mu \cdot \vec{R}_\mu - g_\rho \overline{\psi}_i \gamma^\mu \vec{\tau} \psi_i \cdot \vec{R}^\mu \\ & - \frac{1}{4} F^{\mu\nu} F_{\mu\nu} - e \overline{\psi}_i \gamma^\mu \frac{(1 - \tau_3)}{2} \psi_i A_\mu. \end{aligned} \quad (1)$$

From the above Lagrangian, we obtain the field equations for the nucleons and mesons. These equations are solved by expanding the upper and lower components of the Dirac spinors and the boson fields in an axially deformed harmonic oscillator basis, with an initial deformation  $\beta_0$ . The set of coupled equations are solved numerically by a self-consistent iteration method [54–57]. Based on the effective interactions used in the RMF functional, the center-of-mass energy can be calculated either in harmonic oscillator approximation or from the quasiparticle vacuum self-consistently. In the case of oscillator approximation, the spurious center-of-mass motion is subtracted using the Elliott-Skyrme approximation [58]. The

analytical form is given as:

$$E_{\text{c.m.}} = \frac{3}{4}A^{-\frac{1}{3}}, \quad (2)$$

where  $A$  is the mass number. On the other hand, one should estimate the center-of-mass energy using the self-consistent method [59,60],

$$E_{\text{c.m.}} = \frac{\langle F | P^2 | F \rangle}{2M}, \quad (3)$$

where  $|F\rangle = |F\rangle_{\text{RMF}}$  wave function.  $P$  and  $A$  are the total linear momentum and the nuclear mass number, respectively. The results obtained from these two methods for Zr isotopes are given in Table I. From the table it is clear that the calculated center-of-mass energies from both the cases are almost overlap with each other. Hence, one can use any one of the method for the center-of-mass energy correction in the calculation of this nuclear mass region (see Ref. [60]). The total quadrupole deformation parameter  $\beta_2$  is evaluated from the resulting proton and neutron quadrupole moments, as

$$Q = Q_n + Q_p = \sqrt{\frac{16\pi}{5}} \left( \frac{3}{4\pi} A R^2 \beta_2 \right). \quad (4)$$

The root-mean-square (rms) matter radius is defined as

$$\langle r_m^2 \rangle = \frac{1}{A} \int \rho(r_\perp, z) r^2 d\tau, \quad (5)$$

where  $A$  is the mass number, and  $\rho(r_\perp, z)$  is the axially deformed density. The total binding energy and other observables are also obtained by using the standard relations, given in Ref. [49]. As outputs, we obtain different potentials, densities, single-particle energy levels, radii, deformations, and the binding energies. For a given nucleus, the maximum binding energy corresponds to the ground state and other solutions are obtained as various excited intrinsic states.

### A. Pairing energy

To deal the nuclear bulk properties of open-shell nuclei, one can not neglect the pairing correlation in their ground and intrinsic excited state [61]. Various methods, such as the BCS approach, the Bogoliubov transformation, and the particle number conserving methods, have been developed to treat the pairing effects in the study of nuclear properties including fission barriers [62–65]. In principle, the Bogoliubov transformation is a widely used method to take pairing correlation into account for the drip-line region [39–42,66,67]. In the case of nuclei not too far from the  $\beta$ -stability line, one can use the constant gap BCS pairing approach reasonably well to take care of pairing [68]. Further, the BCS approach may fail for neutron-rich light nuclei. In the present analysis, we have considered the intermediate mass neutron-rich nuclei,

hence the RMF results with BCS treatment should be reliable. In other words, to avoid the difficulty in the calculation, one can employ the constant gap BCS approach to deal with the present mass region [51,69,70]. Now the expression for pairing energy is given by

$$E_{\text{pair}} = -G \left[ \sum_{i>0} u_i v_i \right]^2, \quad (6)$$

where  $v_i^2 + u_i^2 = 1$  is known as the occupation probability and  $G$  is the pairing force constant [71–73]. The variational procedure with respect to the occupation numbers  $v_i^2$ , gives the BCS equation  $2\epsilon_i u_i v_i - \Delta(u_i^2 - v_i^2) = 0$  and the pairing gap  $\Delta$  is defined by

$$\Delta = G \sum_{i>0} u_i v_i. \quad (7)$$

This is the famous BCS equation for pairing energy. The densities are contained within the occupation number,

$$n_i = v_i^2 = \frac{1}{2} \left[ 1 - \frac{\epsilon_i - \lambda}{\sqrt{(\epsilon_i - \lambda)^2 + \Delta^2}} \right]. \quad (8)$$

The standard expression for the pairing gaps of proton and neutron are  $\Delta_p = RB_s e^{sI-tI^2}/Z^{1/3}$  and  $\Delta_n = RB_s e^{-sI-tI^2}/A^{1/3}$ , respectively [69]. Here the constants and their values are as follows:  $R = 5.72$ ,  $s = 0.118$ ,  $t = 8.12$ ,  $B_s = 1$ , and  $I = (N - Z)/(N + Z)$ . (Note that the gaps obtained by these expressions are valid for nuclei both on or away from the stability line for this mass region.) The pairing force constant  $G$  is not calculated explicitly from the RMF equations. Using the above gap parameter, we calculate the occupation probability and the chemical potentials  $\lambda_n$  and  $\lambda_p$  from the particle numbers using the above equations. Now, we can rewrite the pairing energy as,

$$E_{\text{pair}} = -\frac{\Delta^2}{G} = -\Delta \sum_{i>0} u_i v_i. \quad (9)$$

Since it depends on the occupation probabilities  $v_i^2$  and  $u_i^2$ , the pairing energy should change with particle number for a constant pairing gap. It is well known that the pairing energy  $E_{\text{pair}}$  diverges if it is extended to an infinite configuration space for a constant pairing gap  $\Delta$  and force constant  $G$ . Also, for the states spherical or deformed, with large momenta near the Fermi surface,  $\Delta$  decreases in all the realistic calculations with finite range forces. However, for the sake of simplicity of the calculation, we have assumed the pairing gap for all states is equal near the Fermi surface. In the present calculations we have used a pairing window, and all the equations extended up to the level  $\epsilon_i - \lambda \leq 2(41A^{1/3})$ , where a factor of 2 has been included in order to reproduce the pairing correlation energy for neutrons in  $^{118}\text{Sn}$  using Gogny force [71,72]. This kind of approach has already been used by many other authors in RMF and Skyrme-Hartree-Fock (SHF) models [51,52,71,72].

### III. DETAILS OF CALCULATION AND RESULTS DISCUSSION

In the present work, we have used the successful NL3 [74] and the recently proposed NL3\* [75] force parameters, which are excellent in the description of ground and excited states with many collective aspects for spherical and deformed nuclei. In the mean time, there are several other mean-field interactions that have been developed. In particular, the density-dependent meson-exchange DD-ME1 [46] and DD-ME2 [76] interactions, which are adjusted to improve the isovector channel. Further, the density-dependent points coupling interaction [34,77] has been developed to describe the deformed heavy and superheavy nuclei. Even these interactions have been developed to provide a very successful description of various special features. At present, the NL3 [74] and NL3\* [75] forces are also accepted in competition with these parameters to reproduce the properties of the stable and nuclei far from the  $\beta$ -stability line. In RMFT, the mean-field equations are solved self-consistently by taking different inputs of the initial deformation called  $\beta_0$  [49,51,71,74,75]. To verify the convergence of the ground-state solutions for this mass region, we pursued the calculation for  $N_B = 20$  and varying  $N_F$  from 10–22. The difference between the binding energy obtained from  $N_F = 18$  to  $N_F = 10$ –22 is entitled as relative binding energy difference and denoted as  $(\Delta E)_B$ . The estimated relative binding energy difference  $(\Delta E)_B = E_B(N_F = 18) - E_B(N_F = 10\text{--}22)$ , the charge radius  $r_{ch}$ , and the quadruple deformation  $\beta_2$  for  $^{100,126}\text{Zr}$ ,  $^{102,128}\text{Mo}$ ,  $^{104,130}\text{Ru}$ , and  $^{106,132}\text{Pd}$  isotopes from NL3 and NL3\* force are shown in Fig. 1. From the figure, it is clear that the variations of these solutions are  $\leq 0.02\%$  on binding energy and  $0.01\%$  on nuclear radii over the range of major shell fermions  $N_F$  from 10–14. But these relative changes are reduced to  $\leq 0.002\%$  on binding energy and  $0.001\%$  on nuclear radii for

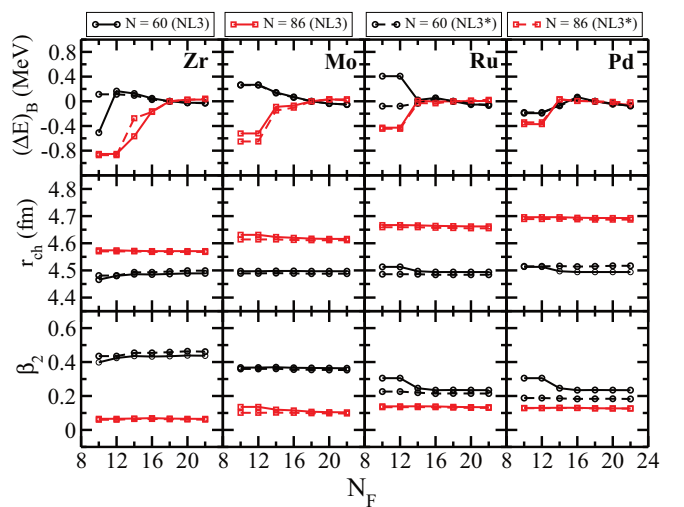


FIG. 1. (Color online) The obtained results for nuclear relative binding energy difference  $(\Delta E)_B = E_B(N_F = 18) - E_B(N_F = 10\text{--}22)$ , charge radius  $r_{ch}$  and the quadruple deformation  $\beta_2$  for  $^{100,126}\text{Zr}$ ,  $^{102,128}\text{Mo}$ ,  $^{104,130}\text{Ru}$ , and  $^{106,132}\text{Pd}$  isotopes from NL3 and NL3\* force parameter. See text for more details.

$N_F$  values from 14–22. Hence, the desired number of major shells for fermions and bosons are  $N_F = 18$  and  $N_B = 20$  for the considered mass region. However, the number of mesh points for Gauss-Hermite and Gauss-Lagurre integration are 20 and 24, respectively. For a given nucleus, the solution corresponding to maximum binding energy is treated as a ground state and other solutions are the intrinsic excited states of the nucleus.

### A. Potential energy surface

Conventionally, in the case of a quantum mechanical system, the path followed by the different solutions at various deformations define a potential barrier or potential energy surface, which can be used for the determination of the ground state of a nucleus. More elaborately, from the potential energy surface (PES) obtained from a self-consistent relativistic mean-field theory, one can regulate the reasonable results for the ground state similar to the nonrelativistic calculations [78]. Since quadrupole deformation plays the most important and dominant part, we have neglected the other deformation coordinates in the present study for simplicity and low computation time cost. Here, the potential energy curve is calculated microscopically by the constrained RMF theory [51,52,79–81]. The expectation value of the Hamiltonian [61,71,80] at certain deformation is given as

$$H' = \sum_{ij} \frac{\langle \psi_i | H_0 - \lambda Q_2 | \psi_j \rangle}{\langle \psi_i | \psi_j \rangle}, \quad (10)$$

where  $\lambda$  is the constraint multiplier and  $H_0$  is the Dirac mean-field Hamiltonian. The convergence of the numerical solutions on the binding energy and the deformation are not very much sensitive to the deformation parameter  $\beta_0$  of the harmonic oscillator basis for the considered range due to the large basis. Thus, the deformation parameter  $\beta_0$  of the harmonic oscillator basis is chosen near the expected deformation to obtain high accuracy and less computation time period.

The potential energy surface as a function of deformation parameter  $\beta_2$ , for the proton rich nucleus  $^{82}\text{Zr}$ , the double magic nucleus  $^{90}\text{Zr}$  and the neutron-rich nucleus  $^{110,120}\text{Zr}$  are shown in Fig. 2 as a representative case. All other Mo–, Ru–, and Pd– isotopes are also showing similar behaviors, which are not given here. The energy ( $E_b = E_{g.s.} - E_{e.s.}$ ) on the  $Y$  axis is the difference between the ground-state energy to other constraint energy solutions. The solid and dotted lines in the figure are for NL3 and NL3\* force, respectively. The calculated PES for both the cases are shown for a wide range from oblate to prolate deformations. We notice from the figure that more than one minima appear at different  $\beta_2$ . The magnitude of binding energy for the corresponding minima shows that the ground-state solution appears at a certain value of  $\beta_2$ . The  $\beta_2$  for the ground state is not same for all isotopes of Zr (see Tables II and III). For example, the ground-state solutions for  $^{82}\text{Zr}$ ,  $^{90}\text{Zr}$ ,  $^{110,120}\text{Zr}$ , and  $^{120}\text{Zr}$  are  $\sim -0.2$ ,  $0.0$ ,  $0.4$ , and  $0.0$ , respectively. One can find similar nature for both the force parameters, hence one can conclude that the ground-state properties of these nuclei are independent of the force parameters used.

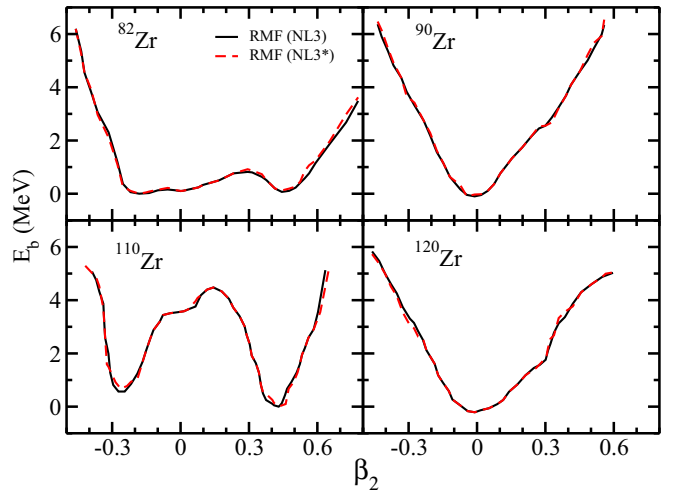


FIG. 2. (Color online) The potential energy surface of  $^{82,90,110,120}\text{Zr}$  as a function of quadrupole deformation parameter  $\beta_2$  for both NL3 and NL3\* forces in axially deformed relativistic mean field calculations.

### B. Nuclear binding energy and quadrupole deformation

The calculations mainly explain the nuclear structure as well as the substructure properties, based on the basic ingredients, such as binding energy ( $E_B$ ), quadrupole moment  $Q_{20}$ , nucleonic density distribution  $\rho(r_{\perp}, z) = \rho_p(r_{\perp}, z) + \rho_n(r_{\perp}, z)$ , and rms nuclear radii, etc. Nevertheless, the present study demonstrates the applicability of RMF on the nuclear structure study for transition nuclei near the neutron drip line. The obtained results for binding energy BE, the quadrupole deformation parameter  $\beta_2$ , and the charge radius  $r_{ch}$  for NL3 and NL3\* force parameters for the isotopic chain of Zr, Mo, Ru, and Pd are listed in Tables II and III along with the experimental data [82]. It is worth mentioning that the obtained results from the NL3 force parameter almost matches to the mass table by Lalazissis *et al.* [50] except for a few nuclei, though the small differences are acceptable in the accuracy of mean-field level. Further, we notice on the binding energy and the rms  $r_{ch}$  for all nuclei over the isotopic chain from RMF agree well with the experimental values. Quantitatively, the mean deviation of BE and  $r_{ch}$  between the calculated result and the available experimental data over the isotopic chain are  $\sim 0.01$  and  $0.004$ , respectively. Further, the quadrupole deformation parameter  $\beta_2$ , for both ground state (g.s.) and selective excited states (e.s.) are also given in Tables II and III. In some of the earlier RMF and Skyrme Hartree-Fock (SHF) calculations, it was shown that the quadrupole moment obtained from these theories reproduce the experimental data pretty well [37,51,52,66,71,74,83–85]. From the table, one can find that the shape of a few nuclei is not consistent with the experimental observed shape. In this context, we have also estimated that the first excited state solutions for these nuclei correspond to the experimental deformations (see Tables II and III). A careful inspection to these solutions shows that the small difference in the binding energy is an indication of shape coexistence. In other words, the two solutions in these nuclei are almost degenerate and

TABLE II. The binding energy  $E_B$ , root-mean-square charge radius  $r_{ch}$ , and the quadrupole deformation parameter  $\beta_2$  for the ground states and few selective first intrinsic excited state of  $^{82-126}\text{Zr}$  and  $^{86-130}\text{Ru}$  nuclei compared with the experimental data [82] wherever available. See the text for more details.

N	RMF (NL3)			RMF (NL3*)			Experiment			RMF (NL3)			RMF (NL3*)			Experiment			
	BE	$r_{ch}$	$\beta_2$	BE	$r_{ch}$	$\beta_2$	BE	$r_{ch}$	$\beta_2$	BE	$r_{ch}$	$\beta_2$	BE	$r_{ch}$	$\beta_2$	BE	$r_{ch}$	$\beta_2$	
$^{82-126}\text{Zr}$																			
42	691.3	4.29	-0.197	690.9	4.29	-0.192				0.367	698.7	4.39	-0.204	698.1	4.39	-0.199			
	691.0	4.28	0.488	690.6	4.28	0.488													
44	715.7	4.29	-0.188	715.8	4.27	-0.001				0.251	726.8	4.39	0.053	726.8	4.38	0.058			
	715.5	4.28	0.469	715.5	4.28	0.467													
46	739.2	4.28	0.001	739.2	4.27	0.001	740.6		0.151	755.7	4.39	0.096	755.5	4.38	0.089				
48	762.6	4.28	0.001	761.9	4.28	0.001	762.6	4.2812	0.185	782.3	4.37	0.006	782.0	4.37	0.004				
50	783.9	4.28	0.001	783.1	4.28	0.000	783.9	4.2696	0.089	808.0	4.37	0.001	807.4	4.37	0.000	806.9			
52	797.8	4.29	0.001	797.2	4.28	0.000	799.8	4.3057	0.1027	825.6	4.39	0.003	825.1	4.38	0.002	826.5	4.3927	0.1579	
54	810.5	4.34	0.169	808.9	4.31	0.002	814.7	4.3312	0.090	843.2	4.42	0.159	842.5	4.42	0.155	844.8	4.4232	0.1947	
56	824.5	4.38	0.243	822.9	4.38	0.233	828.9	4.3498	0.080	860.1	4.45	0.205	859.2	4.44	0.199	861.9	4.4536	0.2148	
58	837.0	4.42	0.318	834.9	4.40	0.274	840.9	4.4185		875.3	4.47	0.225	874.3	4.47	0.216	877.9	4.4818	0.2404	
60	849.8	4.48	0.432	847.6	4.49	0.453	852.2	4.5220	0.355	889.3	4.49	0.234	888.2	4.48	0.215	893.0	4.5104	0.2707	
62	860.6	4.50	0.428	858.2	4.50	0.428	863.7	4.5690	0.427	903.9	4.57	0.385	901.7	4.52	0.295	907.5		0.257	
64	870.6	4.52	0.427	868.0	4.52	0.424	873.8		0.38	917.6	4.54	-0.236	916.3	4.53	-0.232	920.9		0.292	
										916.9	4.58	0.373	915.8	4.57	0.371				
66	880.4	4.54	0.419	877.6	4.54	0.418	883.9			931.0	4.55	-0.236	929.5	4.55	-0.234	933.3		0.295	
										929.1	4.59	0.357	928.0	4.59	0.357				
68	889.8	4.56	0.416	886.8	4.56	0.419	892.6			943.4	4.57	-0.239	941.5	4.57	-0.238	945.0		0.306	
										941.5	4.60	0.349	940.1	4.60	0.348				
70	897.2	4.59	0.445	893.9	4.59	0.461	900.4			954.1	4.59	-0.233	951.8	4.58	-0.229				
72	904.1	4.62	0.478	900.4	4.62	0.479				963.9	4.59	-0.203	961.5	4.59	-0.196				
74	911.8	4.52	-0.170	908.8	4.52	-0.166				974.2	4.61	-0.178	971.5	4.60	-0.176				
76	917.7	4.52	-0.109	914.5	4.52	-0.095				983.1	4.62	-0.169	979.9	4.61	-0.167				
78	923.4	4.52	0.065	920.0	4.52	0.043				991.6	4.61	0.114	988.7	4.60	0.111				
80	929.6	4.54	0.003	925.7	4.53	0.002				999.5	4.61	0.074	996.2	4.61	0.074				
82	935.6	4.55	0.001	932.0	4.56	0.001				1007.3	4.62	0.001	1003.4	4.61	0.001				
84	936.7	4.56	0.001	932.8	4.57	0.064				1010.1	4.64	0.067	1006.3	4.64	0.076				
86	937.3	4.57	0.069	933.6	4.58	0.079				1013.4	4.66	0.139	1009.4	4.66	0.138				

might have large shape fluctuations. For example, in  $^{82}\text{Zr}$  the two solutions for  $\beta_2 = -0.197$  and  $\beta_2 = 0.25$  are completely degenerate with binding energies of 691.3 and 691.0 MeV, respectively. Hence, the ground state can be changed to the excited state and vice versa by a small change in the input, such as the pairing strength, etc., in the calculations. Similar behavior is also observed for a few other nuclei in the present analysis and are listed in Tables II and III. Such phenomenon is known to exist in many other mass regions of the nuclear chart [86,87].

### C. Two-neutron separation energy $S_{2n}$ ( $Z, N$ )

Two-neutron separation energy  $S_{2n}$  ( $Z, N$ ), can be estimated from the ground-state nuclear binding energies of  $BE(Z, N)$ ,  $BE(Z, N - 2)$  and the neutron mass  $m_n$  with the relation:

$$S_{2n}(Z, N) = -BE(Z, N) + BE(Z, N - 2) + 2m_n. \quad (11)$$

The BE of the  $^A X_Z$  and  $^{A-2} X_Z$  are calculated from RMF for NL3 and NL3\* force parameters. It is essential to have very precise mass measurements to predict the correct estimation of the nucleon separation energy  $S_{2n}$ . The calculated  $S_{2n}$  energy from RMF as a function of neutron number for Zr, Mo, Ru, and

Pd isotopes are compared with latest experimental data [82], shown in the Fig. 3. From the figure, it is clear that in an isotopic chain, the  $S_{2n}$  energy shows the well-known regularities for a given atomic number, i.e., the  $S_{2n}$  decreases smoothly as the number of neutron increases in an isotopic chain. Sharp discontinuities (in other words, kinks) appear at neutron magic numbers at  $N = 50$  and  $82$ . In energy terminology one can say that the energy necessary to remove two neutrons from a nucleus ( $Z, N_{\text{magic}} + 2$ ) is much smaller than that to remove two neutrons from the nucleus ( $Z, N_{\text{magic}}$ ), which breaks the regular trend.

### D. Differential variation of two-neutron separation energy

The differential variation of the two-neutron separation energy ( $S_{2n}$ ) with respect to the neutron number ( $N$ ), i.e.,  $dS_{2n}(N, Z)$  is defined as

$$dS_{2n}(Z, N) = \frac{S_{2n}(Z, N + 2) - S_{2n}(Z, N)}{2}. \quad (12)$$

The  $dS_{2n}(N, Z)$  is one of the key quantities to explore the rate of change of separation energy with respect to the neutron number in an isotopic chain. Here, we calculated the  $dS_{2n}(N, Z)$

TABLE III. Same as Table II, only for  $^{84-128}\text{Mo}$  and  $^{88-132}\text{Pd}$  isotopes.

N	RMF (NL3)			RMF (NL3*)			Experiment			RMF (NL3)			RMF (NL3*)			Experiment		
	BE	$r_{ch}$	$\beta_2$	BE	$r_{ch}$	$\beta_2$	BE	$r_{ch}$	$\beta_2$	BE	$r_{ch}$	$\beta_2$	BE	$r_{ch}$	$\beta_2$	BE	$r_{ch}$	$\beta_2$
$^{84-128}\text{Mo}$																		$^{88-132}\text{Pd}$
42	696.7	4.34	-0.206	696.2	4.34	-0.203				697.8	4.42	0.002	697.8	4.42	0.002			
44	722.4	4.34	0.001	722.6	4.34	0.002	725.8			730.0	4.44	0.094	729.9	4.44	0.095			
46	748.2	4.33	0.003	748.2	4.33	0.003	750.1			760.9	4.43	0.101	760.7	4.43	0.104			
48	773.4	4.33	0.001	773.1	4.33	0.001	773.7			789.5	4.42	0.004	789.1	4.42	0.005			
50	796.9	4.33	0.001	796.4	4.33	0.001	796.5	4.3156	0.1058	817.4	4.42	0.001	816.8	4.41	0.001	815.0		
52	812.7	4.34	0.001	812.2	4.34	0.001	814.2	4.3518	0.1509	836.9	4.43	0.003	836.3	4.42	0.004	836.3		
54	828.1	4.38	0.174	827.1	4.37	0.158	830.8	4.3841	0.1720	855.9	4.46	0.136	855.4	4.46	0.139	856.4		
56	843.5	4.42	0.230	842.2	4.41	0.220	846.2	4.4088	0.1683	874.2	4.48	0.176	873.6	4.48	0.177	875.3	4.4839	0.196
58	857.2	4.45	0.268	855.7	4.43	0.246	860.5	4.4458	0.2309	891.1	4.51	0.189	890.5	4.50	0.188	892.8	4.5086	0.209
60	871.2	4.50	0.366	869.1	4.49	0.356	873.9			906.9	4.52	0.187	906.2	4.52	0.184	909.5	4.5322	0.229
62	883.6	4.53	0.386	881.4	4.52	0.382	886.9			921.8	4.53	0.190	921.1	4.53	0.179	925.2	4.5563	0.243
64	895.4	4.49	-0.234	894.0	4.49	-0.228	898.9			936.1	4.57	0.240	934.9	4.54	0.165	940.2	4.5776	0.257
	895.2	4.54	0.379	893.9	4.54	0.377												
66	907.4	4.51	-0.236	905.7	4.51	-0.233		0.38		951.8	4.59	-0.231	950.4	4.58	-0.229	954.3		0.220
	906.5	4.56	0.374	904.9	4.55	0.373				950.3	4.60	0.292	949.5	4.60	0.290			
68	918.1	4.53	-0.241	915.9	4.53	-0.239				965.7	4.62	-0.23	963.9	4.60	-0.234	967.6		0.164
	927.0	4.55	-0.231	924.6	4.54	-0.223				963.5	4.62	0.304	961.9	4.60	0.301			
70	927.0	4.55	-0.231	924.6	4.54	-0.223				977.9	4.63	-0.221	975.8	4.61	-0.226			0.207
	935.7	4.55	-0.197	933.2	4.55	-0.190				975.3	4.60	0.216	974.1	4.59	0.216			
74	944.6	4.57	-0.180	941.7	4.56	-0.179				989.1	4.63	-0.198	986.8	4.62	-0.184			
76	951.8	4.58	-0.172	948.4	4.58	-0.171				1000.6	4.63	-0.163	998.1	4.62	-0.151			
78	958.4	4.57	0.114	955.0	4.56	0.094				1011.9	4.63	0.115	1009.8	4.62	0.114			
80	965.1	4.58	0.042	961.5	4.57	0.037				1022.8	4.64	0.104	1020.2	4.63	0.105			
82	972.2	4.59	0.002	968.0	4.59	0.001				1032.4	4.65	0.073	1029.3	4.64	0.076			
84	973.7	4.60	0.002	969.6	4.60	0.029				1041.5	4.65	0.001	1037.8	4.65	0.002			
86	975.8	4.62	0.114	971.7	4.61	0.101				1044.5	4.66	0.027	1040.9	4.67	0.043			
	1048.7	4.69	0.130	1045.1	4.69	0.132												

for NL3 and NL3\* force parameters. Further, we have also estimated the  $dS_{2n}$  ( $N, Z$ ) energy from the experimental  $S_{2n}$  energy. In Fig. 4, we compared the experimental values with

our calculation for Zr, Mo, Ru, and Pd isotopes. In general, the large, sharp, deep fall in the  $dS_{2n}$  over an isotopic chain shows the signature of neutron shell closure. In other words, this deviation in the general trend may disclose some additional

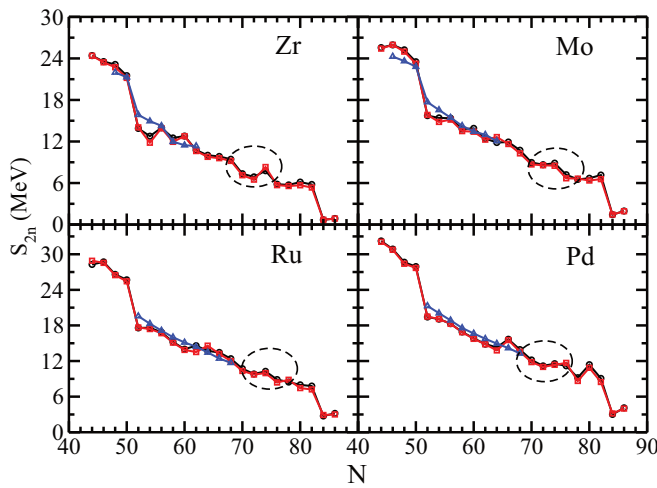


FIG. 3. (Color online) The two-neutron separation energy as a function of neutron number from RMF theory with NL3 and NL3\* force parameter for  $^{82-126}\text{Zr}$ ,  $^{84-128}\text{Mo}$ ,  $^{86-130}\text{Ru}$ , and  $^{88-132}\text{Pd}$  nuclei are compared with the experimental data [82].

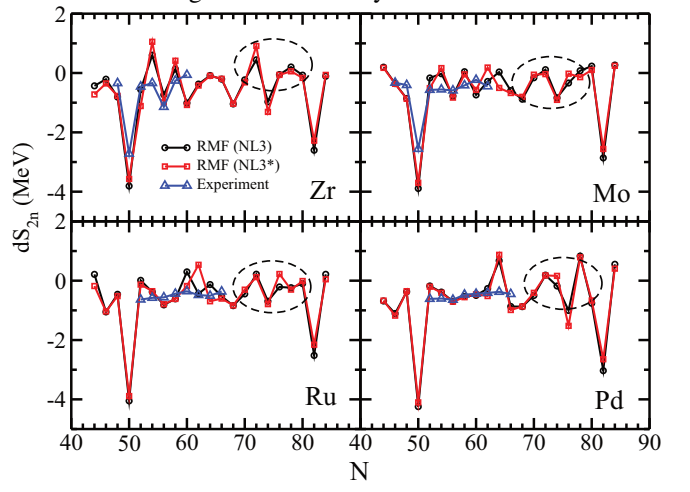


FIG. 4. (Color online) The differential variation of the two-neutron separation energy  $dS_{2n}$  as a function of neutron number from RMF theory with NL3 and NL3\* force parameter for  $^{82-126}\text{Zr}$ ,  $^{84-128}\text{Mo}$ ,  $^{86-130}\text{Ru}$ , and  $^{88-132}\text{Pd}$  nuclei are compared with the experimental data [82].

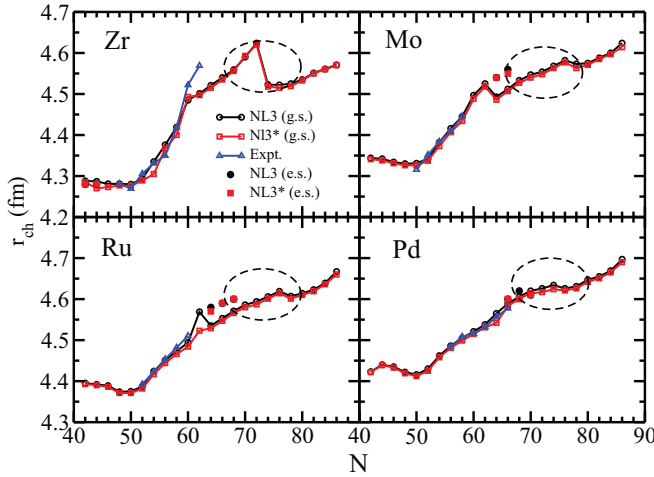


FIG. 5. (Color online) The root-mean-square charge distribution  $r_{ch}$  of  $^{82-126}\text{Zr}$ ,  $^{84-128}\text{Mo}$ ,  $^{86-130}\text{Ru}$ , and  $^{88-132}\text{Pd}$  nuclei from RMF theory with NL3 and NL3\* force parameter are compared with the experimental data [89].

nuclear structure features. From the figure, we observed the same characteristics for all  $Z = 38-46$ .

### E. Root-mean-square charge distributions

The root-mean-square (rms) matter radius from relativistic mean-field theory can be expressed as:

$$\langle r_m^2 \rangle = \frac{1}{A} \int \rho(r_{\perp}, z) r^2 d\tau, \quad (13)$$

where  $A$  is the mass number and  $\rho(r_{\perp}, z)$  is the axially deformed density. The rms charge radius can be calculated from the rms proton radius  $\langle r_p^2 \rangle$  with simple algebraic relation,

$$\langle r_{ch}^2 \rangle = \langle r_p^2 \rangle + 0.64. \quad (14)$$

From the theoretical point of view, the macroscopic-microscopic models [88] and microscopic mean-field formulations using effective interactions are the most sophisticated approaches to determine the rms charge radius in comparison with experimental data [89]. In this present work, we have shown the variations or fluctuations of the charge radii on top of a fairly smooth average behavior in an isotopic chain. The results from RMF approaches for NL3 and NL3\* parameters along with the available experimental data are shown in Fig. 5. From the figure it is clear that the obtained radii from RMF for  $^{82-126}\text{Zr}$ ,  $^{84-128}\text{Mo}$ ,  $^{86-130}\text{Ru}$ , and  $^{88-132}\text{Pd}$  follows closely the experimental data [89]. For most of the nuclei, the experimental values are unavailable; the RMF predictions are made for the charge radius of such a nucleus that awaits experimental confirmation. The circle, square, and triangle symbols indicate the ground-state data for NL3, NL3\*, and experiment, respectively. Further, the solid circle and solid square symbols indicate the shapes correspond to the first intrinsic excited states obtained from NL3 and NL3\* forces. From the figure, one can observe the smooth behavior for lighter isotopes, then there is a small drop in the charge radii for Zr, Mo, and Pd at about  $N = 62, 64, 72$ , and  $74$ . This drop

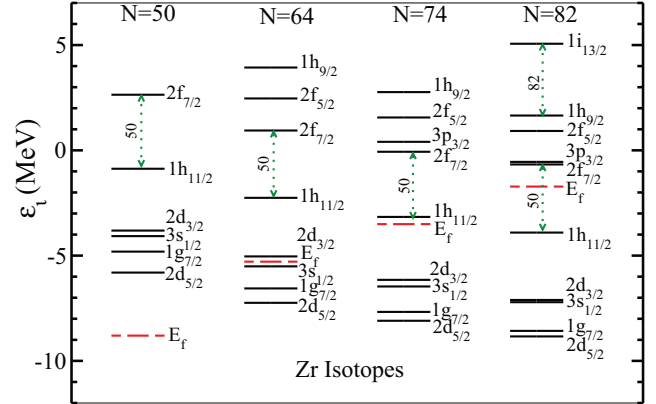


FIG. 6. (Color online) The single-particle energy levels  $\epsilon_i$  for  $^{90}\text{Zr}$ ,  $^{104}\text{Zr}$ ,  $^{114}\text{Zr}$ , and  $^{122}\text{Zr}$  from RMF model with NL3 force parameter

corresponds to the transition from the prolate to the oblate and vice versa. But the magnitude for both the states are different, i.e., the oblate deformation is at  $\beta_2 \sim -0.2$  while the prolate one appears with  $\beta_2 \sim 0.4$ . In the case of the Pb isotope, the change is the radii only at one place, i.e., at  $N = 74$ . Further, one can notice that the tiny change in the calculation can lead to the first intrinsic excited state as a ground state (see Fig. 2). In other words, we can practically degenerate the ground-state binding energy for the deformation corresponding to the first intrinsic excited state. Thus, the inconsistency in the  $r_c^2$  could be explained in terms of configuration mixing, i.e., the actual ground state is not only the spherical configuration but also from the neighboring deformed intrinsic excited states.

### F. Single-particle energy levels

In the above analysis, we found some signatures of shell closures at  $N = 82$  for all these isotopic chains. As a further confirmatory test, the single-particle energy levels for neutrons in isotopic chains are examined. The obtained single-particle levels  $\epsilon_i$  for even isotopes of Zr near Fermi level are shown in Fig. 6 for NL3 force as an ideal case. However, we have obtained similar results for all isotopic chains from NL3 and NL3\* force parameters. We observed the large gap at  $N = 82$ , near the drip-line region. In general, the spin-orbit splitting of the levels are scaled down for neutron-rich nuclei, but  $1h_{11/2}$  level (at  $N = 82$ ) is higher in the Zr nuclei studied. Quantitatively, in  $^{122}\text{Zr}$ , the  $\Delta\epsilon_i = \epsilon_i(1i_{13/2}) - \epsilon_i(1h_{9/2})$  at  $N = 82$  is 4.5 MeV, which is a considerably large value compare to the neighbor splitting. Almost identical behavior is noticed for the isotopic chain of Mo, Ru, and Pd nucleus at  $N = 82$ , irrespective of the force parameter used. Such a rearrangement of the single-particle orbitals at  $N = 82$ , well accepted the shell closure at  $N = 82$  for the considered transitional nuclei.

### G. Contour plot of the axially deformed densities

In the above figures and tables, we have shown the results some of the structural observables such as binding energy,

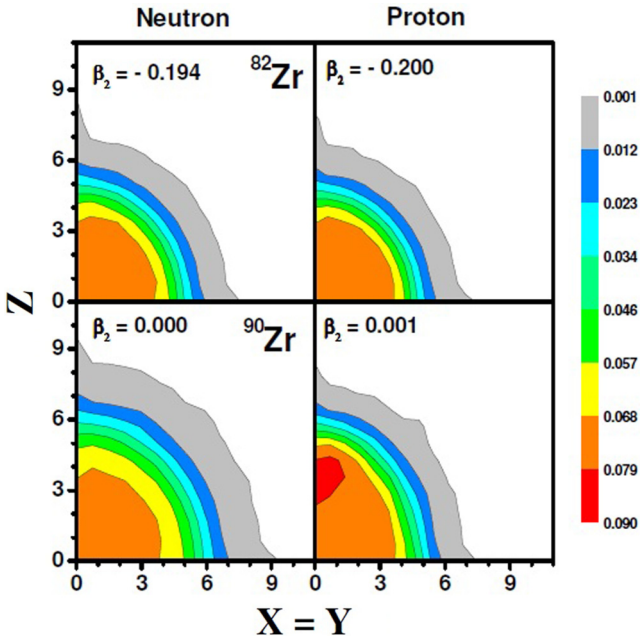


FIG. 7. (Color online) The contour plot of the axially deformed ground-state density distribution of proton and neutron for  $^{82}\text{Zr}$  and  $^{90}\text{Zr}$ .

quadrupole deformation, root-mean-square radius, separation energy, differential separation energy, and single-particle energy levels in comparison with the experimental data [82,89], wherever available. Here, we have focused on the ground of  $^{82-126}\text{Zr}$ ,  $^{84-128}\text{Mo}$ ,  $^{86-130}\text{Ru}$ , and  $^{88-132}\text{Pd}$  nuclei along with a few selectively excited states. Based on these structural observables, we found some significant signatures of the shell closure at  $N = 82$  (drip-line region) in the isotopic chains. Further, the abnormal change in the  $S_{2n}$  and  $dS_{2n}$  in the isotopic chain of Zr, Mo, and Ru nucleus suggests a shape coexistence at  $N \sim 64$  and 74. This divergence over an isotopic chain can be cut down by taking the dynamical correlations beyond mean field [90–92].

To get a complete picture of the reason behind such discrepancy over the isotopic chain, we have shown the contour plot of the axially deformed density of protons and neutrons of these nuclei. In Figs. 7 and 8, we have displayed the distribution of Zr isotopes for  $N = 42, 50, 60$ , and  $82$  as representative cases. All the isotopes of Mo, Ru, and Pd also show similar behavior to Zr as shown in Figs. 7 and 8. From the figure, one can clearly identify the spherical, oblate, prolate shapes corresponding to their  $\beta_2$  values as the local minima in the PECs. Similar calculations can also be found in Refs. [93,94]. In these figures, we can see the transition from oblate to prolate at  $N = 42$ , then the change to the spherical structure at  $N = 50$ , and further changing the deformations to prolate ones. Even though the proton number is fixed in the isotopic chain, still we found a little change in the density distribution due to the influence of excess neutron number. Following the color code, the red and light gray color correspond to the high density ( $\sim 0.09 \text{ fm}^{-3}$ ) and low density ( $\sim 0.001 \text{ fm}^{-3}$ ), respectively. More inspection of the figures shows that the

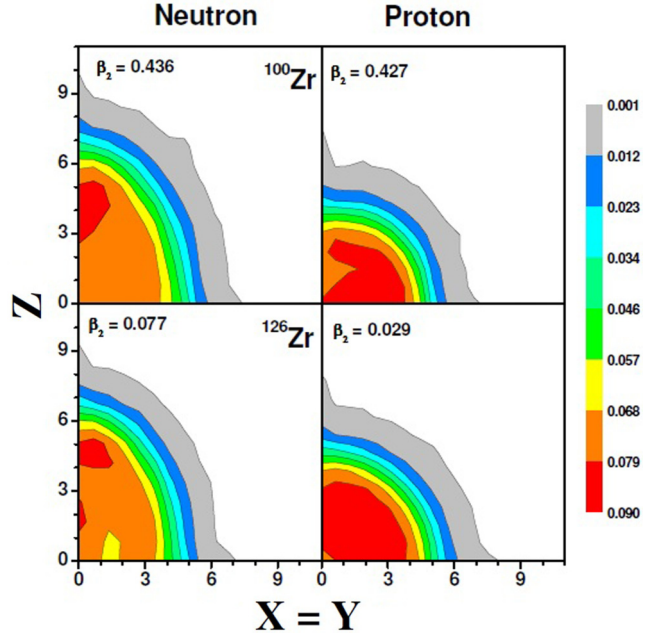


FIG. 8. (Color online) The contour plot of the axially deformed ground-state density distribution of proton and neutron for  $^{100}\text{Zr}$  and  $^{126}\text{Zr}$ .

central density of the proton increases as compared to the neutron with respect to the neutron number. In this region, few isotopes of Mo (for  $^{116-118}\text{Mo}$ ) are the triaxial shape in their ground state, which is very close to the axial solutions [94]. In other words, the location of minima for a triaxial solution for these isotopes of Mo are almost same as the minima appear for an axial prolate solution. Hence, we have used the simple axial deformed calculation, which is adequate for a qualitative description of structural observables in this mass region.

#### IV. SUMMARY AND CONCLUSIONS

We have used self-consistent relativistic mean-field theory with the most popular NL3 and recent NL3\* force parameters to study the structural evolution in transition nuclei. The conjecture has been made from the binding energy, neutron separation energies, differential variation of separation energy, the root-mean-square charge radii, and the single-particle energy levels of these nuclei. In the present calculations we have shown that Zr, Mo, and Ru isotopes undergo a transition from oblate to prolate shapes at  $N \sim 64$  and 74. But, the case of Pd follows a smooth pattern throughout the isotopic chain. We have also shown that the dependence of nuclear charge radii on deformation also plays a crucial role on their structural transition. Further, we have also observed a large shell gap at  $N = 82$  near the drip-line region, almost the same in magnitude at  $N = 50$  for these considered nuclei, which is a well-known feature for mean-field calculation. We have also demonstrated the efficiency of RMF theory calculations to reproduce those features and therefore to make predictions in unexplored regions.

## ACKNOWLEDGMENTS

The author thanks S. K. Patra, Institute of Physics, Bhubaneswar and Shan-Gui Zhou, Institute of Theoretical

Physics, Chinese Academy of Sciences for various discussions regarding this work. Further, the author is thankful to Cheng-Jun Xia, Jie Zhao, Bing Wang, Mung Xu, and Zhen-Hua Zhang for careful reading of the manuscript.

- 
- [1] M. Pfützner, M. Karny, L. Grigorenko, and K. Riisager, *Rev. Mod. Phys.* **84**, 567 (2012).
- [2] B. Blank and M. Borge, *Prog. Part. Nucl. Phys.* **60**, 403 (2008).
- [3] E. Olsen, M. Pfützner, N. Birge, M. Brown, W. Nazarewicz, and A. Perhac, *Phys. Rev. Lett.* **110**, 222501 (2013).
- [4] H. J. Rose and G. A. Jones, *Nature (London)* **307**, 245 (1984).
- [5] Raj K. Gupta and W. Greiner, *Int. J. Mod. Phys.* **03**, 335 (1994).
- [6] B. B. Singh, M. Bhuyan, S. K. Patra, and Raj K. Gupta, *J. Phys. G: Nucl. Part. Phys.* **39**, 025101 (2012).
- [7] L. P. Gaffney *et al.*, *Nature (London)* **497**, 199 (2013).
- [8] C. J. (Kim) Lister and Jonathan Butterworth, *Nature (London)* **497**, 190 (2013).
- [9] C. Thibault *et al.*, *Phys. Rev. C* **12**, 644 (1975).
- [10] O. B. Tarasov *et al.*, *Phys. Rev. Lett.* **102**, 142501 (2009).
- [11] T. Ohnishi *et al.*, *J. Phys. Soc. Jpn.* **77**, 083201 (2008).
- [12] T. Ohnishi *et al.*, *J. Phys. Soc. Jpn.* **79**, 073201 (2010).
- [13] H. Watanabe *et al.*, *Phys. Rev. Lett.* **111**, 152501 (2013).
- [14] J. Meng and P. Ring, *Phys. Rev. Lett.* **80**, 460 (1998).
- [15] H. Iwasaki *et al.*, *Phys. Lett. B* **481**, 7 (2000).
- [16] T. Motobayashi *et al.*, *Phys. Lett. B* **346**, 9 (1995).
- [17] B. Bastin *et al.*, *Phys. Rev. Lett.* **99**, 022503 (2007).
- [18] M. G. Mayer, *Phys. Rev.* **75**, 1969 (1949).
- [19] J. Blons, *Nucl. Phys. A* **502**, 121 (1989).
- [20] T. Sumikama, K. Yoshinaga, H. Watanabe, S. Nishimura, Y. Miyashita, K. Yamaguchi, K. Sugimoto, J. Chiba, Z. Li, H. Baba *et al.*, *Phys. Rev. Lett.* **106**, 202501 (2011).
- [21] ISOLDE/IS333, t ISOLDE/IS333, and IS393 Collaborations, K.-L. Kratz, B. Pfeiffer, O. Arndt, S. Hennrich, and A. Wöhr, *Eur. Phys. J. A* **25**, 633 (2005).
- [22] S. Nishimura, *Prog. Theor. Exp. Phys.* **2012**, 03C006 (2012).
- [23] X. L. Tu *et al.*, *Phys. Rev. Lett.* **106**, 112501 (2011).
- [24] Y. H. Zhang *et al.*, *Phys. Rev. Lett.* **109**, 102501 (2012).
- [25] W. D. Myers, *Nucl. Phys. A* **145**, 387 (1970).
- [26] W. D. Myers and K. H. Schmidt, *Nucl. Phys. A* **410**, 61 (1983).
- [27] I. Tanihata, H. Hamagaki, O. Hashimoto, Y. Shida, N. Yoshikawa, K. Sugimoto, O. Yamakawa, T. Kobayashi, and N. Takahashi, *Phys. Rev. Lett.* **55**, 2676 (1985).
- [28] M. Lassaut and R. J. Lombard, *Z. Phys. A* **341**, 125 (1992).
- [29] T. Burvenich, M. Bender, J. A. Maruhn, and P.-G. Reinhard, *Phys. Rev. C* **69**, 014307 (2004).
- [30] V. Blum, J. Maruhn, P.-G. Reinhard, and W. Greiner, *Phys. Lett. B* **323**, 262 (1994).
- [31] M. Bender, P.-H. Heenen, and P.-G. Reinhard, *Rev. Mod. Phys.* **75**, 121 (2003).
- [32] H.-F. Lü, L.-S. Geng, and J. Meng, *Chin. Phys. Lett.* **23**, 2940 (2006).
- [33] H. Abusara, A. V. Afanasjev, and P. Ring, *Phys. Rev. C* **82**, 044303 (2010).
- [34] B.-N. Lu, E.-G. Zhao, and S.-G. Zhou, *Phys. Rev. C* **85**, 011301(R) (2012).
- [35] V. Prassa, T. Nikšić, G. A. Lalazissis, and D. Vretenar, *Phys. Rev. C* **86**, 024317 (2012).
- [36] V. Prassa, T. Nikšić, and D. Vretenar, *Phys. Rev. C* **88**, 044324 (2013).
- [37] B. D. Serot and J. D. Walecka, *Adv. Nucl. Phys.* **16**, 1 (1986).
- [38] P. G. Reinhard, *Rep. Prog. Phys.* **52**, 439 (1989).
- [39] P. Ring, *Prog. Part. Nucl. Phys.* **37**, 193 (1996).
- [40] D. Vretenar, A. V. Afanasjev, G. A. Lalazissis, and P. Ring, *Phys. Rep.* **409**, 101 (2005).
- [41] J. Meng, H. Toki, S. G. Zhou, S. Q. Zhang, W. H. Long, and L. S. Geng, *Prog. Part. Nucl. Phys.* **57**, 470 (2006).
- [42] N. Paar, D. Vretenar, and G. Colo, *Rep. Prog. Phys.* **70**, 691 (2007).
- [43] B. A. Nikolaus, T. Hoch, and D. G. Madland, *Phys. Rev. C* **46**, 1757 (1992).
- [44] T. Burvenich, D. G. Madland, J. A. Maruhn, and P.-G. Reinhard, *Phys. Rev. C* **65**, 044308 (2002).
- [45] C. Fuchs, H. Lenske, and H. H. Wolter, *Phys. Rev. C* **52**, 3043 (1995).
- [46] T. Nikšić, D. Vretenar, P. Finelli, and P. Ring, *Phys. Rev. C* **66**, 024306 (2002).
- [47] J. Boguta and A. R. Bodmer, *Nucl. Phys. A* **292**, 413 (1977).
- [48] R. Brockmann and H. Toki, *Phys. Rev. Lett.* **68**, 3408 (1992).
- [49] W. Pannert, P. Ring, and J. Boguta, *Phys. Rev. Lett.* **59**, 2420 (1987).
- [50] G. A. Lalazissis, S. Raman, and P. Ring, *Atm. Data. Nucl. Data. Table.* **71**, 1 (1999).
- [51] S. K. Patra, M. Bhuyan, M. S. Mehta, and Raj K. Gupta, *Phys. Rev. C* **80**, 034312 (2009).
- [52] M. Bhuyan, S. K. Patra, and Raj K. Gupta, *Phys. Rev. C* **84**, 014317 (2011).
- [53] T. Nikšić, D. Vretenar, and P. Ring, *Prog. Part. Nucl. Phys.* **66**, 519 (2011).
- [54] C. J. Horowitz and B. D. Serot, *Nucl. Phys. A* **368**, 503 (1981).
- [55] J. Boguta, *Nucl. Phys. A* **372**, 386 (1981).
- [56] C. E. Price and G. E. Walker, *Phys. Rev. C* **36**, 354 (1987).
- [57] J. Fink, V. Blum, P.-G. Reinhard, J. A. Maruhn, and W. Greiner, *Phys. Lett. B* **218**, 277 (1989).
- [58] J. P. Elliott and T. H. R. Skyrme, *Proc. R. Soc. London A* **232**, 561 (1955).
- [59] Y. Sugahara and H. Toki, *Nucl. Phys. A* **579**, 557 (1994).
- [60] W. Long, J. Meng, N. Van Giai, and S.-G. Zhou, *Phys. Rev. C* **69**, 034319 (2004).
- [61] S. Karatzikos, A. V. Afanasjev, G. A. Lalazissis, and P. Ring, *Phys. Lett. B* **689**, 72 (2010).
- [62] J. Y. Zeng and T. S. Cheng, *Nucl. Phys. A* **405**, 1 (1983).
- [63] H. Molique and J. Dudek, *Phys. Rev. C* **56**, 1795 (1997).
- [64] Z.-H. Zhang, J.-Y. Zeng, E.-G. Zhao, and S.-G. Zhou, *Phys. Rev. C* **83**, 011304(R) (2011).
- [65] T. V. Nhan Hao, P. Quentin, and L. Bonneau, *Phys. Rev. C* **86**, 064307 (2012).
- [66] G. A. Lalazissis, D. Vretenar, P. Ring, M. Stoitsov, and L. M. Robledo, *Phys. Rev. C* **60**, 014310 (1999).
- [67] G. A. Lalazissis, D. Vretenar, and P. Ring, *Nucl. Phys. A* **650**, 133 (1999).

- [68] J. Dobaczewski, H. Flocard, and J. Treiner, *Nucl. Phys. A* **422**, 103 (1984).
- [69] D. G. Madland and J. R. Nix, *Nucl. Phys. A* **476**, 1 (1988).
- [70] P. Möller and J. R. Nix, *At. Data and Nucl. Data Tables* **39**, 213 (1988).
- [71] Y. K. Gambhir, P. Ring, and A. Thimet, *Ann. Phys. (NY)* **198**, 132 (1990).
- [72] S. K. Patra, *Phys. Rev. C* **48**, 1449 (1993).
- [73] M. A. Preston and R. K. Bhaduri, *Structure of Nucleus* (Addison-Wesley, Boston, 1982); Chap. 8, p. 309.
- [74] G. A. Lalazissis, J. König, and P. Ring, *Phys. Rev. C* **55**, 540 (1997).
- [75] G. A. Lalazissis, S. Karatzikos, R. Fossion, D. Pena Arteaga, A. V. Afanasjev, and P. Ring, *Phys. Lett. B* **671**, 36 (2009).
- [76] G. A. Lalazissis, T. Nikšić, D. Vretenar, and P. Ring, *Phys. Rev. C* **71**, 024312 (2005).
- [77] T. Nikšić, D. Vretenar, and P. Ring, *Phys. Rev. C* **78**, 034318 (2008).
- [78] N. Dubray, H. Goutte, and J.-P. Delaroche, *Phys. Rev. C* **77**, 014310 (2008).
- [79] V. Blum, J. Fink, P.-G. Reinhard, J. A. Maruhn, and W. Greiner, *Phys. Lett. B* **223**, 123 (1989).
- [80] D. Hirata, H. Toki, I. Tanihata, and P. Ring, *Phys. Lett. B* **314**, 168 (1993).
- [81] B. N. Lu, J. Zhao, E. G. Zhao, and S. G. Zhou, *Phys. Rev. C* **89**, 014323 (2014).
- [82] M. Wang, G. Audi, A. H. Wapstra, F. G. Kondev, M. MacCormick, X. Xu, and B. Pfeiffer, *Chen. Phys. C* **36**, 1603 (2012).
- [83] B. A. Brown, *Phys. Rev. C* **58**, 220 (1998).
- [84] S. K. Patra, C.-L. Wu, C. R. Praharaj, and R. K. Gupta, *Nucl. Phys. A* **651**, 117 (1999).
- [85] P. Arumugam, B. K. Sharma, S. K. Patra, and R. K. Gupta, *Phys. Rev. C* **71**, 064308 (2005).
- [86] S. Yoshida, S. K. Patra, N. Takigawa, and C. R. Praharaj, *Phys. Rev. C* **50**, 1398 (1994).
- [87] S. K. Patra, S. Yoshida, N. Takigawa, and C. R. Praharaj, *Phys. Rev. C* **50**, 1924 (1994).
- [88] J. S. Wang, W. Q. Shena, Z. Y. Zhua, J. Feng, Z. Y. Guob, W. L. Zhan, G. Q. Xiao, X. Z. Cai, D. Q. Fang, H. Y. Zhang, and Y. G. Ma, *Nucl. Phys. A* **691**, 618 (2001).
- [89] I. Angeli and K. P. Marinova, *Atomic Data and Nucl. Data Tables* **99**, 69 (2013).
- [90] M. Bender, G. F. Bertsch, and P.-H. Heenen, *Phys. Rev. C* **73**, 034322 (2006).
- [91] M. Bender, G. F. Bertsch, and P.-H. Heenen, *Phys. Rev. C* **78**, 054312 (2008).
- [92] J.-P. Delaroche *et al.*, *Phys. Rev. C* **81**, 014303 (2010).
- [93] E. Bauge *et al.*, *Europhys. J. A* **48**, 113 (2012).
- [94] R. Rodriguez-Guzmn, P. Sarriiguren, L. M. Robledob, and S. Perez-Martin, *Phys. Lett. B* **691**, 202 (2010).